Calibrating 100 years of polar faculae measurements: implications for the evolution of the heliospheric magnetic field

Andrés Muñoz-Jaramillo

Harvard-Smithsonian Center for Astrophysics, Cambridge, MA 02138, USA

University Corporation for Atmospheric Research, Boulder, CO 80307, USA

Department of Physics & Astronomy, University of Utah, Salt Lake City, UT 84112, USA

amunoz@cfa.harvard.edu

and

Neil R. Sheeley, Jr.

Space Science Division, Naval Research Laboratory, Washington, DC 20375-5352, USA

neil.sheeley@nrl.navy.mil

and

Jie Zhang

School of Physics, Astronomy and Computational Sciences, George Mason University, Fairfax, VA 22030, USA

jzhang7@gmu.edu

and

Edward E. DeLuca

Harvard-Smithsonian Center for Astrophysics, Cambridge, MA 02138, USA

edeluca@cfa.harvard.edu

ABSTRACT

In addition to the well known 11-year periodicity, the solar cycle also presents long-term modulations of its amplitude and period which remain poorly understood. Although the current solar cycle picture places a lot of importance in the evolution of the polar magnetic field (as the source of the toroidal bundles from

which active regions emerge), there is still no consolidated database which can be used to study the evolution of the polar magnetic field spanning the timescales necessary to understand long-term solar variability. In this paper we show how we can address this deficiency by consolidating Mount Wilson Observatory polar faculae data from four data reduction campaigns (1906-1964, Sheeley 1966; 1960-1975, Sheeley 1976; 1975-1990, Sheeley 1991; 1985-2007, Sheeley 2008), validating it through a comparison with facular data counted automatically from MDI intensitygrams, and calibrating it against polar field measurements taken by the Wilcox Solar Observatory (1977-2011) and average polar field and total polar flux calculated using MDI line-of-sight magnetograms (1996-2011). Our results show that the consolidated polar facular measurements are in excellent agreement with both polar field and polar flux estimates, making them an ideal proxy to study the evolution of the polar magnetic field since 1906. Additionally, we combine this database with sunspot area measurements to study the role of the polar magnetic flux in the evolution of the heliospheric magnetic field (HMF) and find that, taken together, polar flux and sunspot area play a better role at explaining the evolution of the HMF during the last century than sunspot area alone. The best fit to HMF is obtained by using a linear combination of the square root of these quantities.

Subject headings: Sun: activity – Sun: faculae, plages – Sun: magnetic fields – Sun: dynamo

1. Introduction

Solar faculae are bright features on the surface of the Sun associated with accumulations of magnetic flux inside inter-granular lanes (Hale 1922). They are believed to be the consequence of a depression in the optical surface of the Sun caused by the magnetic field, which allows the observer to see the warmer (and thus brighter) walls of the granular upflows (Spruit 1976, 1977; Keller et al. 2004); making them easier to spot near the solar limb. As a result of this physical relationship, it is not surprising that faculae can be used to track magnetic flux making them a very good proxy for the evolution of surface magnetic fields. In fact, their numbers – measured on white light photographs taken by the Mount Wilson Observatory (MWO) – have been found to be modulated by the solar cycle (Sheeley 1964, 1966) and there is a strong correlation between polar facular count and the polar line-of-sight (LOS) magnetic field observed by the Wilcox Solar Observatory (WSO; Sheeley 1991, 2008). This, and the ability to see them clearly at the poles, makes faculae as valuable for

studying the poloidal aspect of the solar cycle as sunspots are for the toroidal part. The standardization, validation, and magnetic calibration of a polar faculae dataset spanning the hundred years of MWO white light photographs is the goal of this study.

2. Cross-Calibration of MWO Polar Faculae Measurements

In this work we use MWO polar facular measurements taken in four different data reduction campaigns (1906-1964, Sheeley 1964, 1966; 1960-1975, Sheeley 1976; 1970-1990, Sheeley 1991; and 1985-2007, Sheeley 2008). Two sets of high-quality white light photographs were selected during each data reduction campaign, each corresponding to the intervals when the solar poles are most visible from Earth (Feb-15 to Mar-15 for the south pole and Aug-15 to Sep-15 for the north pole). The five best images were selected for each interval based on image quality, photographic contrast, and (whenever possible) that such high-quality images be uniformly spaced in time. Polar faculae were counted based on eye estimates of bright features whose contrasts were comparable to those of low latitude faculae, but whose sizes were much smaller. To remove possible chronological biases, the spring and fall decks on each campaign were shuffled before obtaining the facular count, after which the dates of observation were recorded. Subsequently, the five facular numbers measured for each interval were averaged into a single data point corresponding to each interval. In our study we use only the facular measurements for the dominant pole of each deck (south and north poles respectively for the spring and fall decks). Note that though facular measurements are a strictly positive quantity, they have been given a sign (which reverses when they reach a minimum), matching the sign of the dominant magnetic field believed (or known) to be present at each pole during each polar cycle. This allows for easier visualization and comparison with signed quantities like magnetic field and flux and removes discontinuities in slope that occur when the field goes through zero. However, this sign is not taken into consideration when comparing different facular measurements.

As can be seen in Figure 1, data taken during each subsequent campaign was ensured to have an overlap with the previous campaign, but there seems to be an underestimation of facular count when one compares each subsequent campaign with the previous one. This discrepancy is relatively small between the 1st and 2nd campaigns and the 2nd and 3rd campaigns, but it is larger between the 3rd and 4th campaigns, as shown in Figure 2. It is difficult to estimate exactly the source of this discrepancy given the subjective nature of the process of facular selection, but some factors that may be playing a role include the fact that the 4th observational campaign was performed in a different room (involving a different light box and different viewing conditions) and that the observer's criteria for discriminating

faculae may have become stricter with the pass of time. Fortunately, the goodness of a linear fit through each overlap (0.99 for 1st vs. 2nd, 0.80 for 2nd vs. 3rd, and 0.94 for 3rd vs. 4th) suggests that these discrepancies can be corrected with a multiplicative factor corresponding to the slope of the linear fit. Furthermore, the fact that the 3rd and 4th observations are well within the interval of WSO observations allows us to verify that this correction is quite adequate in the case of the campaigns with the biggest discrepancy (3rd and 4th; see Figure 11). In this work we use the 95% confidence intervals as a measure of the error in the multiplicative factors and calibrate all data reduction campaigns to the 3rd campaign in order to minimize error propagation.

The adequacy of the multiplicative correction is further confirmed in Figure 3, where we can observe very good agreement across different campaigns. This leaves us with a standardized polar faculae dataset covering more than a century of observations. The following step is to validate the results obtained using this methodology through an automatic algorithm for counting polar faculae on data taken by the Michelson Doppler Imager (MDI; Scherrer et al. 1995). This way we ensure that the MWO facular measurements are robust and not subject to methodological or instrumental errors, as well as validating the number of polar faculae counted in the interval 2002-2008 which were taken after the manufacture of the high-quality film used by the MWO for obtaining the white-light images was discontinued and was no longer available.

3. Validation of Mount Wilson Polar Faculae Measurements using MDI

In this work we use continuum intensitygrams (each image of 1024x1024 pixels from which limb-darkening has been removed; see Figure 4), taken by MDI going from 19-May-1996 to 26-Dec-2010. We use one image per day (when available), counting the number of faculae above (below) 70^oN (70^oS) using an automatic detection code based on that of Zhang, Wang and Liu (2010). The algorithm we use has the following steps:

1. Perform gamma scaling of the image to enhance contrast using the expression $f(x) = k_0 x^\gamma$, where $\gamma = 15$ is the enhancement exponent and $k_0 = 100$ is a normalization constant (See Figs. 5-a & 5-b). The values chosen for the gamma function are specifically tailored with the MDI calibration in mind, which makes the average value of each image very close to 1.

2. Mask pixels above a certain intensity threshold (160.0) which are also located at each pole (See Fig. 5-c). Due to excessive limb brightening in some corrected images, the outer three radial pixels on the solar disk (corresponding to an angular size of 6") are

ignored.

3. Remove single facular pixels in order to distinguish facular regions from small and bright intergranular regions (See Fig. 5-d)

4. Count each isolated facula, fully automatically, independently of the amount of pixels it contains.

After removing overexposed, overcorrected and incomplete images we obtain a daily data series of facular count (see top panels of Figures 6-a & b), to which we apply a month-long running mean (see bottom panels of Figures 6-a & b). This way, we sample a time interval of approximately the same length as the one sampled during the MWO data reduction campaigns (Sheeley 1964, 1966, 1976, & 2008). Finally, in order to validate the Mount Wilson facular count, we select averaged facular counts corresponding to 4-Mar (4-Sep) of each year for the south (north) pole (see Figure 6-c).

As can be seen in Figure 7-a, MWO and MDI facular measurements are in good agreement with the exception of two points (marked with an x in Fig. 7-a); this is likely due to different resulting contrasts in the MDI calibration before and after contact was lost with SOHO. Nevertheless, it is reassuring that results obtained by such different methods differ only by a multiplicative factor (see Fig. 7-a). Furthermore, not only do the measurements agree very well in their actual values, but their relative errors are also essentially the same. This means that even though the Mount Wilson measurements only use five points per averaging month (as opposed to a daily measurement in the MDI facular measurement), they are a representative sample of such an interval and are sufficient to capture polar facular variability in the measuring period. Taken together, these results strongly support the validity and relevance of the combined Mount Wilson dataset. The next natural step now is to use the MWO data to estimate long term evolution of the polar magnetic properties.

4. Comparison Between MWO Facular Measurements, WSO Polar Field Measurements, and MDI LOS Magnetograms

Given that ultimately our objective is to gain insight into the long term evolution of the solar magnetic cycle, it is necessary to evaluate the adequacy of polar facular data as a proxy for polar magnetic field and signed polar magnetic flux. Here, we use polar field measurements taken by the WSO, which have already been correlated favorably with the MWO dataset (Sheeley 2008) – and which have been taken for a period of time coincident with two of the four polar faculae data reduction campaigns – and coincident with MDI

magnetograms which and have directly associated facular measurements. The MDI data are available at a higher cadence (15 per day) and are processed along similar guidelines as MDI intensitygrams.

4.1. Polar Faculae as a Proxy for Polar Magnetic Field Strength

Because WSO magnetic field measurements span 35 years (beginning at 1976; see Figure 8-a), they are ideal as the reference dataset in this subsection. This means that in terms of polar field strength, both the MWO polar faculae measurements and the MDI average polar field measurements are calibrated to their WSO counterparts. In order to develop a consistent set of measurements, we use the average of measurements taken between the 15-Aug and the 15-Sep for the north pole and between 15-Feb and 15-Mar for the south pole (see Figure 8-b).

We also calculate the average polar field strength using MDI line-of-sight (LOS) magnetograms (Figure 9 shows the MDI LOS magnetogram associated with the intensitygram shown in Figure 4). For each day we select one magnetogram (when available) and, whenever possible, one obtained through 5-minute averages since these magnetograms have a better signal to noise ratio. We then calculate the average LOS magnetic field above 70° for the north pole and below -70° for the south pole (see top panels of Figures 10-a & b), perform a month-long running average (see bottom panels of Figures 10-a & b), and select the values of the average polar LOS magnetic field corresponding to 4-Mar (4-Sep) of each year for the south (north) pole (see Figure 10-c). This standardizes the measurements to be consistent with other data used in this work.

As shown in Figure 11-a, polar field measurements taken by the WSO agree very well with the average polar field calculated using MDI. Though values are not identical (WSO measurements are roughly half MDI averages), the difference can be easily corrected through a multiplicative factor and the relationship between them is fit very well by a line that passes through the origin (with a goodness of fit equal to 0.97; see Figure 11-b). A similar result is obtained when comparing WSO magnetic field measurements and MWO facular count, whose relationship is also fit well by a line that passes through the origin (with a goodness of fit equal to 0.90; see Figure 11-a). The general agreement between these quantities is evident in Figure 11-c, which shows their overlap after being corrected by the factors obtained by the linear fits (Figures 11-a & b). In Figure 11-c WSO measurements are joined with a dotted line indicating that they are the reference dataset. The very good agreement between the WSO magnetic field measurements and the facular data belonging to two different MWO data reduction campaigns (after calibration) shows the direct relationship between facular and

magnetic data, and helps validate the calibration process used to standardize the different MWO data reduction campaigns.

4.2. Polar Faculae as a Proxy for Polar Signed Magnetic Flux

Although there is no doubt about the direct relationship between facular measurements and polar field strength, it is useful to study the association with magnetic flux since it is a more relevant quantity for a wide range of studies such as the prediction of the solar cycle amplitude (Choudhuri, Chatterjee & Jiang 2007), modulation of cosmic ray intensity at Earth (see Usosking et al. 2002; Solanki, Schüssler & Fligge 2000; Cliver, Richardson & Ling 2011 and references contained therein), and the understanding of solar wind properties (Luhmann et al. 2009; Wang, Robbrecht & Sheeley 2009). In this section we use MDI LOS magnetograms as the reference dataset because their spatial resolution allows the calculation of signed polar flux. This means that in terms of signed polar flux, both the MWO polar facular measurements and the WSO LOS magnetic field measurements are calibrated to their MDI counterparts. Here we use MDI LOS magnetograms to calculate total signed polar flux using the following steps:

1. Convert MDI LOS magnetic field into radial field assuming that this is the only component of the magnetic field at the surface. To do this we divide the LOS magnetic field by the cosine of the angle between the vector normal to the surface and the vector pointing towards the observer.

2. Calculate the element of area associated with each pixel taking account of the projection effect due to its relative position on the Sun with respect to the observer.

3. Integrate the flux associated with each observed pixel $(B_r A_p)$ for all latitudes above (below) 70° (-70°). The outer three radial pixels on the solar disk (corresponding to an angular size of 6") are ignored in order to reduce the effect of noise (enhanced by the LOS correction) on the polar flux calculation.

The top panels of Figures 12-a & b show the daily values of calculated polar flux. Like the facular count (Figs. 6-a & n) and average polar field (Figs. 10-a & b), there is a clear yearly modulation of polar flux due to the change in observable area above (below) 70° (-70°), though in the case of signed polar flux the modulation is stronger. In order to remove this annual variation, we correct each daily polar flux measurement using a factor equal to the total area of the polar cap divided by the visible area. For consistency with other quantities measured in this work, we define the polar cap as the region in the Sun with a latitude greater

(lower) or equal than 70° (-70°), visible or not. Finally, we perform a month-long running average in order to remain consistent with the time intervals used for other quantities. The result (shown in the bottom panels of Figs. 12-a & b), has a much weaker yearly modulation though it shows clear "pulses" in the standard deviation corresponding to the periods in which the pole in question is barely visible from Earth.

Following the standard procedure in the rest of this work, we select values of polar magnetic flux corresponding to 4-Mar (4-Sep) of each year for the south (north) pole (see Figure 12-c) which we can use to compare to MWO and WSO measurements. Once again we find good agreement between MDI signed polar flux, WSO magnetic field measurements (goodness of fit 0.98; Figure 13-a), and MWO facular count (goodness of fit 0.91; Figure 13-b). This agreement is also evident in an overplot of the three quantities, shown in Figure 13-c, where MDI measurements are joined with a dotted line indicating the fact that they are the reference dataset.

5.   Discussion of Results

After the calibration and validation of the polar faculae database (using data from MDI, WSO and MWO), we are ready to produce a consolidated database for the evolution of the polar magnetic flux since 1906. We use the different calibration factors mentioned in previous sections (referenced to MDI) and select data from MDI (1996-2010), WSO (1975-1996), and MWO (1906-1975); the resultant data series is shown in Figure 14. It is important to mention that due to the necessary propagation of errors incurred in cross-calibrating the MWO data, care must be taken when comparing polar flux values before and after 1975 (as can be observed in Figure 14 from the relative size of the errorbars). However, such a comparison can be done if one allows for a 7% error in this section of the database.

5.1.   Elucidating the Role of the Polar Magnetic Flux in Determining the Properties of the Heliospheric Magnetic Field

It has been found that one of the most important quantities when determining the evolution of geomagnetic activity indicators (which have been measured for more than a century) is the Heliospheric Magnetic Field (HMF; Stamper et al. 1999). This means that not only HMF can act as a meaningful proxy for the long-term evolution of the heliospheric environment, but can also be reconstructed from geomagnetic data all the way to the mid 1800's. Following a decade of vigourous debate, different reconstructions of HMF based on

geomagnetic data have gradually reached consensus (see Lockwood & Owens 2011; Svalgaard & Cliver 2010; and references therein). This reconstructions, which span a similar interval of time as our consolidated magnetic flux dataset, provide us with the opportunity of studying the combined role of active region (AR) and polar flux in determining the characteristics of the heliospheric environment, as well as acting as a consistency check for our polar flux database.

It has been previously shown that HMF scales well as the square root of the sunspot number (acting as a proxy for AR magnetic flux; see Wang, Lean & Sheeley 2005 for more details), and also that during the last four minima HMF correlates well with polar magnetic field (Wang, Robbrecht & Sheeley 2009). This means that both quantities must be playing an important role in determining the evolution of the HMF. However, the lack a of sufficiently long proxy for the evolution of the polar magnetic field has made it difficult to study this relationship in detail. In this section we will address this issue using HMF measurements from the OMNI dataset, HMF reconstructions of Lockwood, Rouillard & Finch (2009), and Svalgaard & Cliver (2010), updated sunspot area data of Balmaceda et al. (2009; sunspot area acts as a better proxy for AR flux than sunspot number does, see Dikpati, de Toma & Gilman 2006; Solanki & Schmidt 1993), and the average of the total signed polar magnetic flux amplitude in both hemispheres.

The correlation of both sunspot area and polar flux with HMF is evident in Figure 15 where we show an overplot of HMF measurements and reconstructions with polar magnetic flux (Fig. 15-a) along with a yearly smoothed total sunspot area. The figure shows clearly how HMF amplitude falls to values dictated by the average polar flux during solar minima (denoted by bracketing black dotted lines), while at the same time it clearly rises and falls with the sunspot cycle. Although both of these matches are evident qualitatively, it is still necessary to demonstrate quantitatively that both polar and AR flux (characterized by sunspot area) have more explanatory power together in terms of the time evolution of HMF than AR flux alone does.

Following the results of Wang, Lean & Sheeley (2005) we make a least-squares fit of sunspot area (as a proxy for AR flux), and the square root of sunspot area to both the reconstructed and measured HMF databases:

$$HMF = a_0 + a_1 SA, \tag{1}$$

$$HMF = a_0 + a_1 \sqrt{SA}, \tag{2}$$

where SA corresponds to sunspot area normalized to its maximum value (such that its maximum value is now 1). We also make a least-squares fit of a linear combination of sunspot area and polar flux (and their square roots) to the reconstructed and measured

HMF databases:

$$HMF = a_0 + a_1 SA + a_2 PF, \tag{3}$$

$$HMF = a_0 + a_1 \sqrt{SA} + a_2 \sqrt{PF}, \tag{4}$$

where PF corresponds to the average of the total signed polar magnetic flux amplitude in both hemispheres normalized to its maximum value (such that its maximum value is now also 1).

We evaluate the performance of these fits by comparing their Root Mean Square Error (RMSE), which is a measure of the average error between a least-squares fit and the fitted data (the smaller the better). As can be observed in Table 1, for all HMF data sources a fit of the square root of sunspot area and polar flux yields a tighter fit than in their linear counterparts (i.e. the models described by Eqs. 2 & 4 perform better). It can also be seen that, in every case, the introduction of polar flux into the fit further reduces RMSE and there is an improvement in the way the fitted function behaves (specially evident during the extended minimum of cycle 23; see Figure 16). However, to ensure that polar and AR flux (characterized by sunspot area) have more explanatory power together (than sunspot area alone), we perform an F-test for each pair of reduced and extended models (Eqs. 1 vs. 3, and Eqs. 2 vs. 4). This way we make sure the improvement in the fit is not simply caused by the increase in fitting parameters. Our null hypothesis is that $a_2 = 0$, or in other words, that the extended model does not provide a significantly better fit than the reduced model. Our test statistic is:

$$F = \frac{(RSS_r - RSS_e)/(n_e - n_r)}{RSS_e/(N - n_e)}, \tag{5}$$

where RSS_r and RSS_e are the residual sum of squares ($RSS = \sum_i^n (y_i - f(x_i))^2$) associated with the reduced (r) and extended (e) models, n_e and n_r are the amount of fitting parameters in each model, and N is the total amount of fitting points. This test statistic quantifies the relationship between the relative decrease in RSS and the relative increase in degrees of freedom. If the null hypothesis is correct, the test statistic has an F distribution with $(n_e - n_r)$ and $(N - n_e)$ degrees of freedom (for more details about the F-test please refer to Snedecor & Cochran 1989).

Our system is described by the following numbers: for our reduced and extended models $n_r = 2$ and $n_e = 3$; for the HMF reconstructions $N = 103$ and for OMNI data $N = 48$. This means that the null hypothesis can be rejected with a statistical significance of 99% if F is greater or equal than 6.89 (7.23) in the case of the HMF reconstructions (OMNI data). Considering that these values are below the F test statistic calculated for the different fits shown in Table 1 (the lowest of which is 17.30 for fits using the square root of sunspot area and polar flux), allows us to reject the null hypothesis and show that polar flux and

sunspot area (as a proxy for AR flux) have more explanatory power together in terms of the time evolution of HMF than AR flux alone does. It is important to note that the performed fits and statistical tests have the added benefit of acting as a sanity check for our calibration across different datasets (MDI, WSO, and MWO) and different data reduction campaigns. However, more important is the establishment of a relationship between one of the quantities most relevant at determining the conditions of the near-Earth environment (HMF) and those directly connected with the long-term evolution of the solar magnetic field. The further refining of this relationship, along with the improvement our models for the evolution of the solar magnetic field, can only improve our understanding the Sun-Earth connection and enhance our space-weather (and space-climate) forecasting capabilities.

6.   Concluding Remarks

The focus of this work has been the standardization, validation and calibration of a long-term facular dataset. For the first part we take advantage of the overlapping intervals across the four different MWO data reduction campaigns and show how, in spite of some underestimation in facular count from one campaign to the next, the discrepancies can be removed by the application of a multiplicative factor (leaving us with a self-consistent database spanning more than a hundred years of observations).

Our second goal was to validate the facular database using two different approaches: the first one is to compare the MWO dataset with an MDI facular count obtained through an automatic detection algorithm; the excellent agreement between MDI and WSO facular count testifies to the validity of the methodology used to count MWO faculae (independently of the fact that it is based on eye estimates). We also compare the MWO standardized facular count belonging to different data reduction campaigns with the LOS magnetic field measurements taken by the WSO. The correspondence between them argues a strong case in favor the adequacy of multiplicative factors as means of standardizing the entire MWO facular dataset.

Given that our ultimate goal is to use MWO facular count as a magnetic proxy, we combine it with MDI total signed polar flux in order to obtain a calibration factor of $(1.04 \pm 0.16) \times 10^{21}$Mx/facula for the standardized facular dataset. It is important to note that this calibration factor does not mean that each polar faculae contains 10×10^{21}Mx, but rather that if one wants to convert the standardized polar facular count into MDI total signed polar flux this is the factor one should use. This calibration factor can in turn be compared with flux measurements of low-latitude faculae as they transit the solar disk (Sheeley 1964, 1966). However, it must be referenced first to the facular values of the first

MWO data reduction campaign (since the standardized facular dataset is referenced to the third MWO data reduction campaign and the MWO estimate was performed during the first data reduction campaign; Sheeley 1964, 1966). When converted to facular values of the first MWO campaign we obtain a factor of $(0.66 \pm 0.20) \times 10^{21}$Mx/facula, which matches well the MWO factor of $(0.34 \pm 0.14) \times 10^{21}$Mx/facula (Sheeley 1966). The reason for the slight overestimation resides in the fact that the MWO estimate is limited exclusively to facular regions whereas we use the entire polar signed flux in our estimate. However, this agreement is highly encouraging because it essentially means that most of the signed flux present in the poles is indeed associated with polar faculae and thus facular count can be used as an excellent proxy of what the poles were doing during more than a hundred years.

Finally, we combine our polar flux database with the sunspot area database of Balmaceda et al. (2009) in order to study the role of the polar flux in the evolution of the heliospheric magnetic field. To do so we perform different fits to the HMF taken from OMNI data, as well as the HMF reconstructions of Lockwood, Rouillard & Finch (2009), and Svalgaard & Cliver (2010). Through the application of an F-test, we find that indeed the combined explicative power of polar flux and sunspot area is larger than sunspot area alone (with a statistical significance higher than 99%). We also find that the best fit to HMF is obtained by using the square root of polar flux and sunspot area (agreeing with the results of Wang, Lean & Sheeley 2005). Considering the causal relationship between the solar surface magnetic field and the evolution of the heliospheric environment, the results of this work represent a step forward towards the practical goal of being able to forecast near-Earth space conditions as our models of the long-term evolution of the surface magnetic field improve; paving the way for a better understanding of long-term solar variability.

7. Acknowledgements

REFERENCES

Balmaceda, L. A., Solanki, S. K., Krivova, N. A., & Foster, S. 2009, J. Geophys. Res., 114, 7104

Choudhuri, A. R., Chatterjee, P., & Jiang, J. 2007, Physical Review Letters, 98, 131103

Cliver, E. W., Richardson, I. G., & Ling, A. G. 2011, Space Sci. Rev., 103

Dikpati, M., de Toma, G., & Gilman, P. A. 2006, Geophys. Res. Lett., 33, 5102

Hale, G. E. 1922, Mon. Not. R. Astron. Soc., 82, 168

Keller, C. U., Schüssler, M., Vögler, A., & Zakharov, V. 2004, Astrophys. J., 607, L59

Lockwood, M. & Owens, M. J. 2011, Journal of Geophysical Research (Space Physics), 116, 4109

Lockwood, M., Rouillard, A. P., & Finch, I. D. 2009, ApJ, 700, 937

Luhmann, J. G., Lee, C. O., Li, Y., Arge, C. N., Galvin, A. B., Simunac, K., Russell, C. T., Howard, R. A., & Petrie, G. 2009, Sol. Phys., 256, 285

Scherrer, P. H., Bogart, R. S., Bush, R. I., Hoeksema, J. T., Kosovichev, A. G., Schou, J., Rosenberg, W., Springer, L., Tarbell, T. D., Title, A., Wolfson, C. J., Zayer, I., & MDI Engineering Team. 1995, Sol. Phys., 162, 129

Sheeley, Jr., N. R. 1964, Astrophys. J., 140, 731

—. 1966, Astrophys. J., 144, 723

—. 1976, J. Geophys. Res., 81, 3462

—. 1991, Astrophys. J., 374, 386

—. 2008, Astrophys. J., 680, 1553

Snedecor, G. W. & Cochran, W. G. 1989, Statistical Methods, 8th edn. (Iowa State University Press)

Solanki, S. K. & Schmidt, H. U. 1993, Astronom. Astrophys., 267, 287

Solanki, S. K., Schüssler, M., & Fligge, M. 2000, Nature, 408, 445

Spruit, H. C. 1976, Sol. Phys., 50, 269

—. 1977, Sol. Phys., 55, 3

Stamper, R., Lockwood, M., Wild, M. N., & Clark, T. D. G. 1999, J. Geophys. Res., 104, 28325

Svalgaard, L. & Cliver, E. W. 2010, Journal of Geophysical Research (Space Physics), 115, 9111

Usoskin, I. G., Mursula, K., Solanki, S. K., Schüssler, M., & Kovaltsov, G. A. 2002, Journal of Geophysical Research (Space Physics), 107, 1374

Wang, Y., Robbrecht, E., & Sheeley, N. R. 2009, Astrophys. J., 707, 1372

Wang, Y.-M., Lean, J. L., & Sheeley, Jr., N. R. 2005, Astrophys. J., 625, 522

Zhang, J., Wang, Y., & Liu, Y. 2010, Astrophys. J., 723, 1006

Fits to $\sqrt{SA}$ and $\sqrt{PF}$

HMF dataset	Sunspot Area Only			Sunspot Area + Polar Flux				F-Test
	a_0	a_1	RMSE (nT)	a_0	a_1	a_2	RMSE (nT)	($F_{99\%} \geq 6.89$)
Fits of SA and PF								
OMNI dataset	5.35	3.09	0.70	3.93	4.06	2.03	0.56	25.29
Lockwood et al. (2009)	5.19	3.98	0.72	4.63	4.45	1.07	0.68	10.68
Svalgaard & Cliver (2010)	5.27	3.84	0.61	4.64	4.37	1.19	0.56	19.21
Fits of $\sqrt{SA}$ and $\sqrt{PF}$								
OMNI dataset	4.49	3.67	0.64	2.03	4.76	2.68	0.48	36.95
Lockwood et al. (2009)	4.23	4.38	0.69	2.97	5.06	1.57	0.64	17.30
Svalgaard & Cliver (2010)	4.35	4.21	0.60	3.04	4.92	1.63	0.53	27.28

Table 1: Fit parameters of sunspot area (left group, Eqs. 1 & 2) and polar flux (middle group, Eqs. 3 & 4) to the different HMF databases used in this work. The top part of the table corresponds to fits of sunspot area and polar flux (Eqs. 1 & 3), the bottom part corresponds to fits of the square roots of those same quantities (Eqs. 2 & 4). RMSE corresponds to the Root Mean Square Error (also referred to as Root Mean Square Deviation), which is a measure of the average error between a least-squares fit and the fitted data (the smaller this quantity is, the better the fit is). The left column shows the values of the F-test used to evaluate whether polar flux and sunspot area have more explanatory power than sunspot area alone; any value of F above 6.89 permits us to reject the null hypothesis that the improvement of the larger model (fitting of both sunspot are and polar flux) is caused by the increase in fitting parameters with a statistical significance of 99%. Note that the null hypothesis can be rejected in every case.
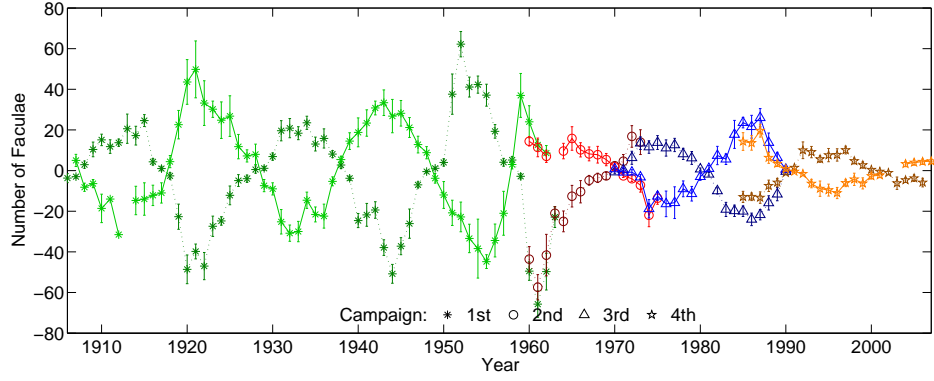
Fig. 1.— Raw MWO Facular measurements. Each campaign is marked with a different color and marker: green asterisk (1st), red circle (2nd), blue triangle (3rd), and orange star (4th). Measurements for the north (south) pole are shown using a dark dashed (light solid) line. After each minima the sign is reversed to match the polarity of each magnetic cycle.
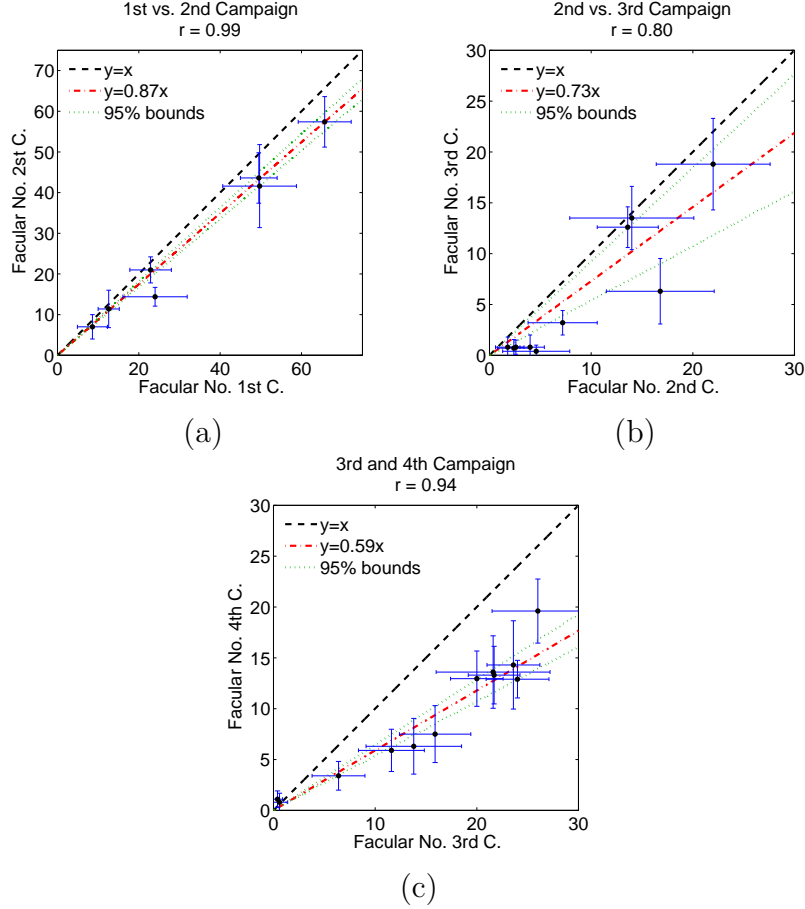
Fig. 2.— (a) Scatter plot comparing MWO facular measurements across data reduction campaigns: (a) 1st vs. 2nd, (b) 2nd vs. 3rd, and (c) 3rd vs. 4th. Each scatter plot is fitted with a line passing through the origin (dot-dashed red). The 95% confidence interval is bounded by dotted green lines and a line of slope one is plotted in dashed black for reference. The factors used to calibrate the data across different campaigns are: 0.87 ± 0.03 between the 1st and 2nd, 0.73 ± 0.19 between 2nd and 3rd, and 0.59 ± 0.05 between 3rd and 4th. They correspond to the slopes and the 95% confidence interval of their respective linear fits.
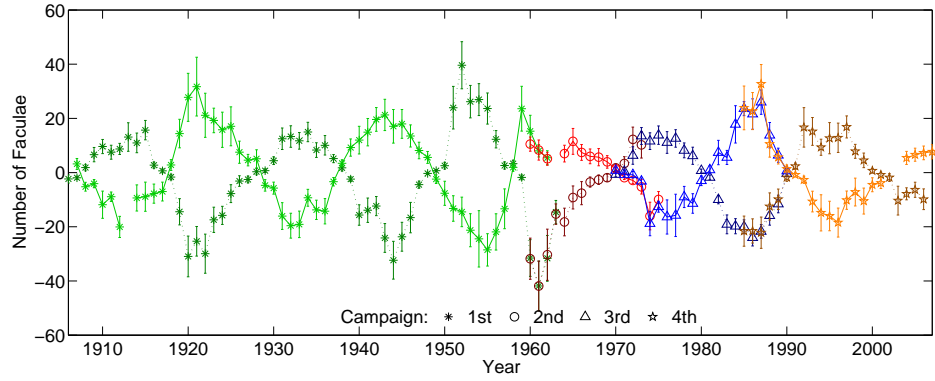
Fig. 3.— Calibrated MWO Facular measurements. Each campaign is marked with a different color and marker: green asterisk (1st), red circle (2nd), blue triangle (3rd), and orange star (4th). Measurements for the north (south) pole are shown using a dark dashed (light solid) line. All campaigns are calibrated to the 3rd campaign.
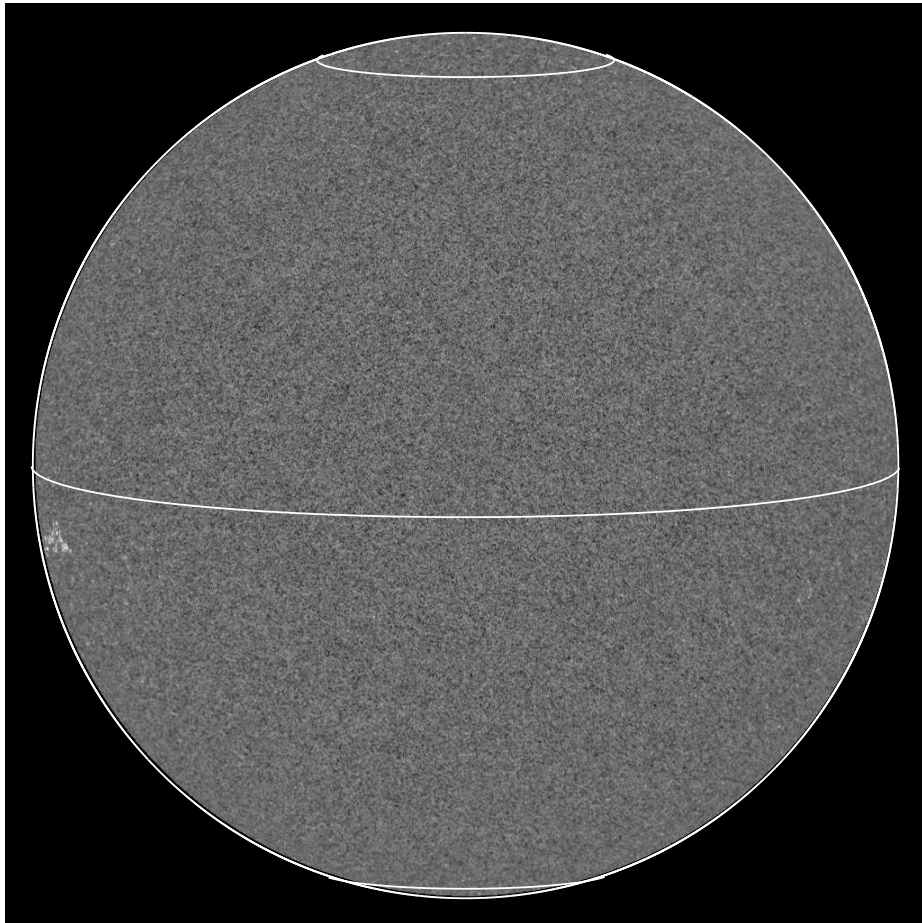
Fig. 4.— MDI 2.0 intensitygram taken on 20-Aug-2007. The circles shown in the image correspond to 70°, 0° and -70° in heliographic latitude.
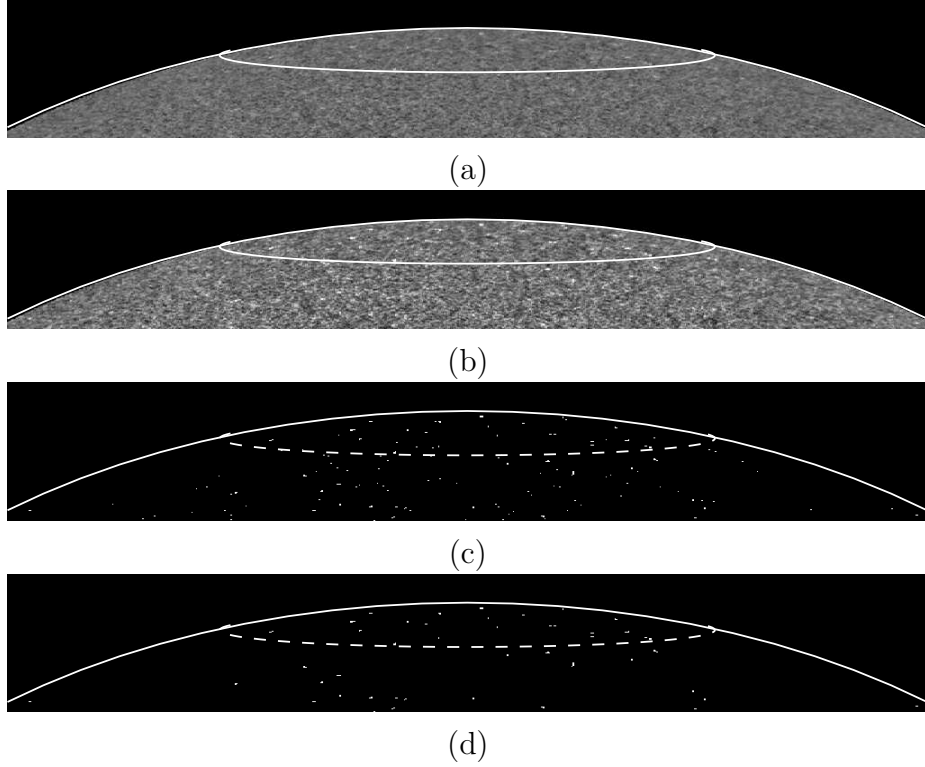
Fig. 5.— Steps in the automatic detection of polar faculae. First the MDI data (a) are scaled using a gamma function (b). Then a mask is built based on a threshold (c) and filtered for individual pixels (d). Polar faculae are counted automatically above 70° for the north pole and below -70° for the south pole. The images show a 70° latitude line for illustration purposes.
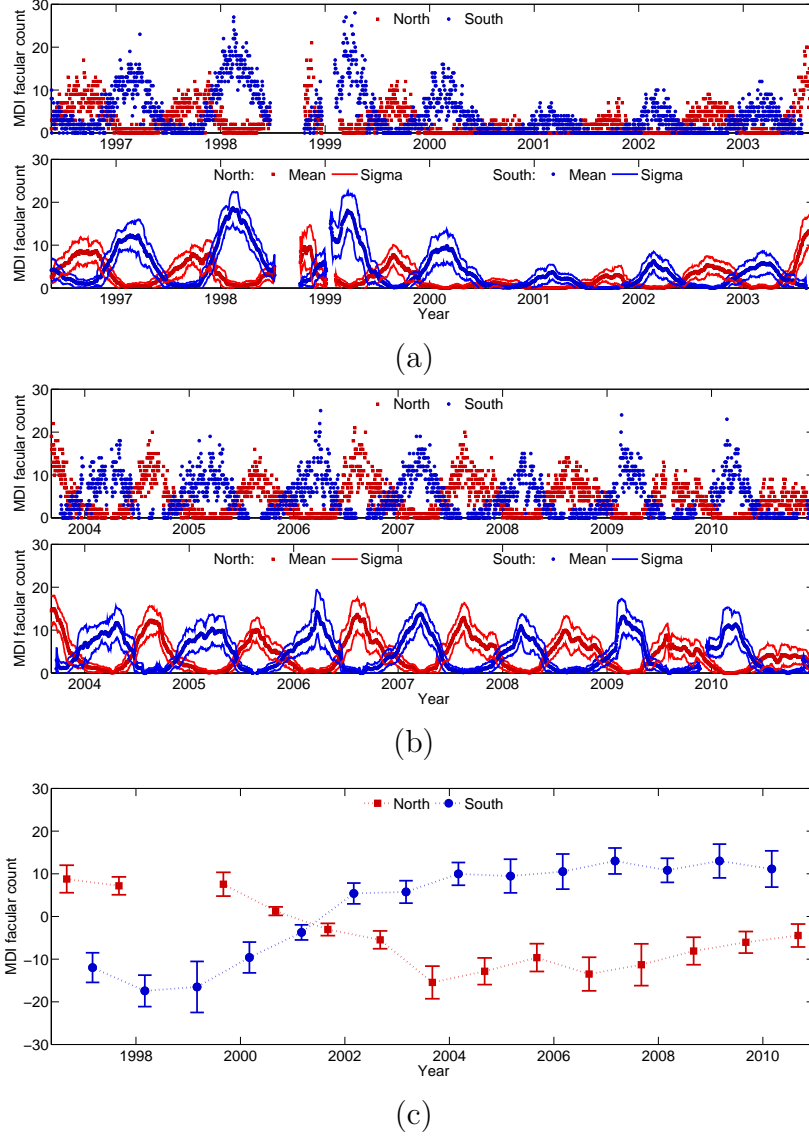
Fig. 6.— MDI facular count for the 1996-2004 (a) and 2004-2011 (b) intervals. The top panel of each figure shows the daily facular count; the bottom panel shows facular count after being applied a month-long running average. Red (blue) corresponds to the north (south) pole and the thin lines correspond to one standard deviation. (c) Selected facular averages for the 1996-2011 interval. Points corresponding to the 4-Mar (4-Sep) of each year are used for the south (north) pole. These dates correspond to the point in Earth's orbit with the best observations of each particular pole.

(a)   (b)
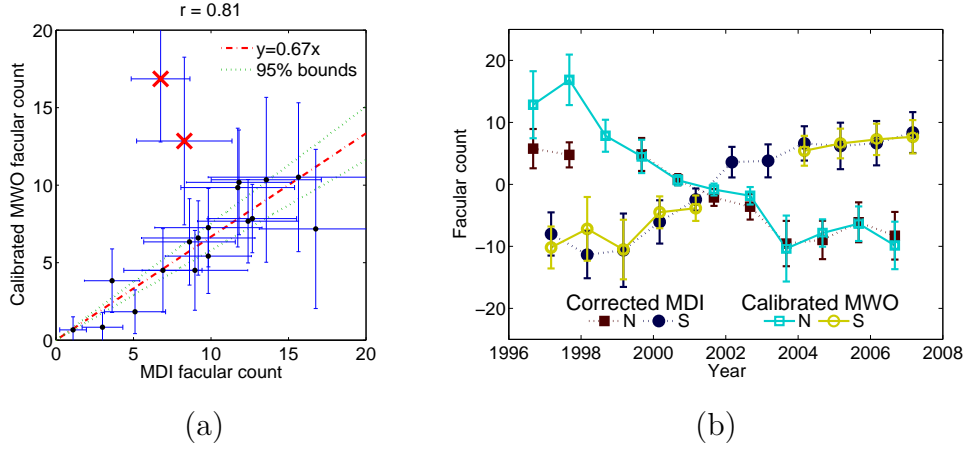
Fig. 7.— (a) Scatter plot comparing MDI and Mount Wilson facular measurements. The data (minus outliers) are fit very well ($r = 0.81$) by a line with a slope of 1.06 which passes trough the origin. (b) Overplot of the calibrated Mount Wilson and the MDI corrected facular measurements. MDI measurements are corrected by a factor of 0.67 ± 0.08 in the figure corresponding to the slope and the 95% confidence interval of the linear fit. The outliers are clearly observed as the MDI facular measurements of 1996 and 1997.

(a)

(b)
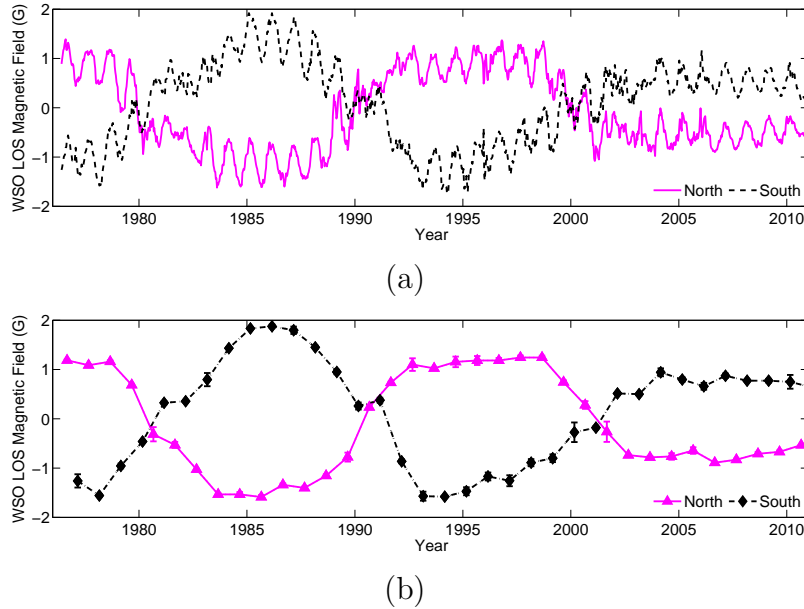
Fig. 8.— (a) Wilcox solar observatory measurements of the polar field. A solid magenta (black dashed) line corresponds to the north (south) pole magnetic field. (b) Selected polar field averages. Points corresponding to the 4-Mar (4-Sep) of each year are used for the south (north) pole. These dates are chosen for consistency and comparison with other datasets.
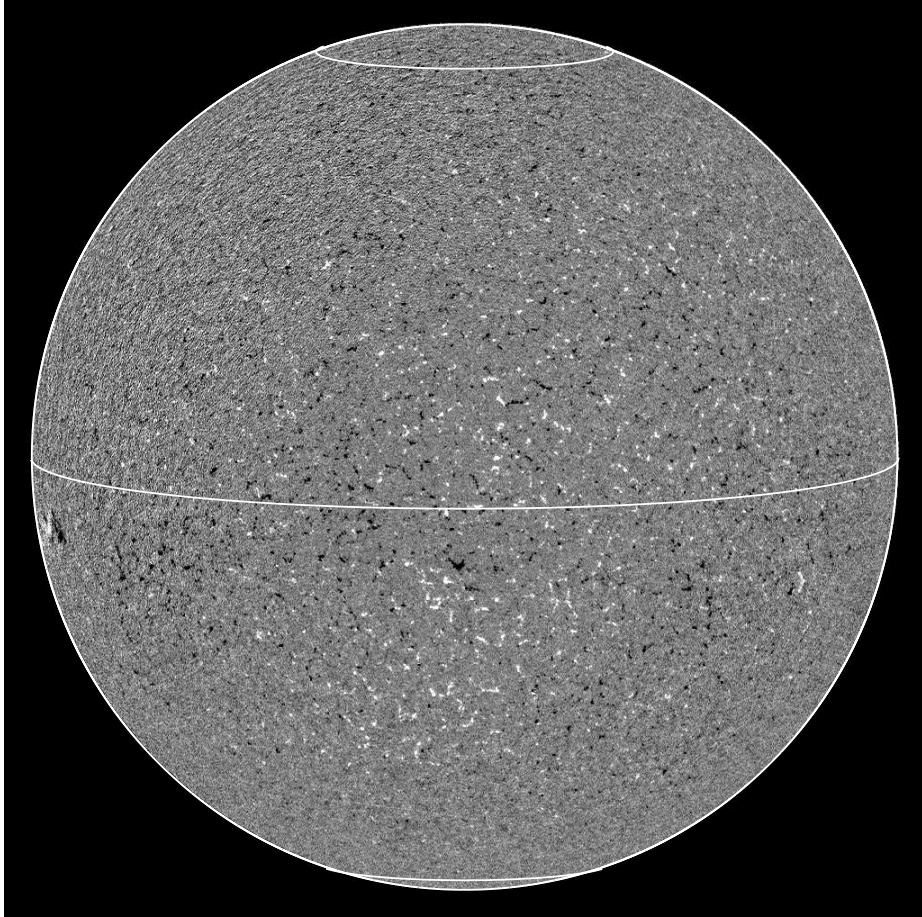
Fig. 9.— MDI 1.8 line-of-sight magnetogram taken on 20-Aug-2007. The circles shown in the image correspond to 70°, 0° and -70°. Colors are saturated in order to enhance visibility of polar patches of magnetic field.
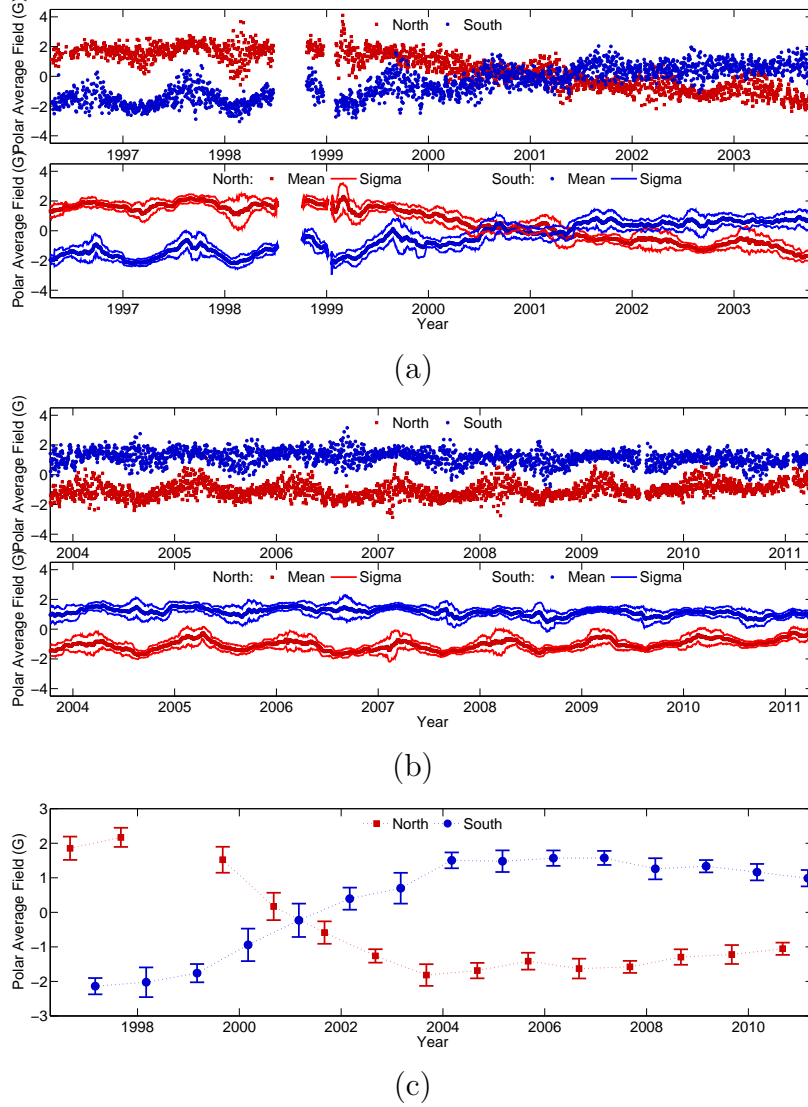
Fig. 10.— MDI average LOS magnetic above field above (below) 70° (-70°) for the 1996-2004 (a) and 2004-2011 (b) intervals. The top panel of each figure shows the daily average field; the bottom panel shows average field after being applied a month-long running average. Red (blue) corresponds to the north (south) pole and the thin lines correspond to one standard deviation. (c) Selected values of the average LOS magnetic field for the 1996-2011 interval. Points corresponding to the 4-Mar (4-Sep) of each year are used for the south (north) pole. These dates correspond to the point in Earth's orbit with the best observations of each particular pole.
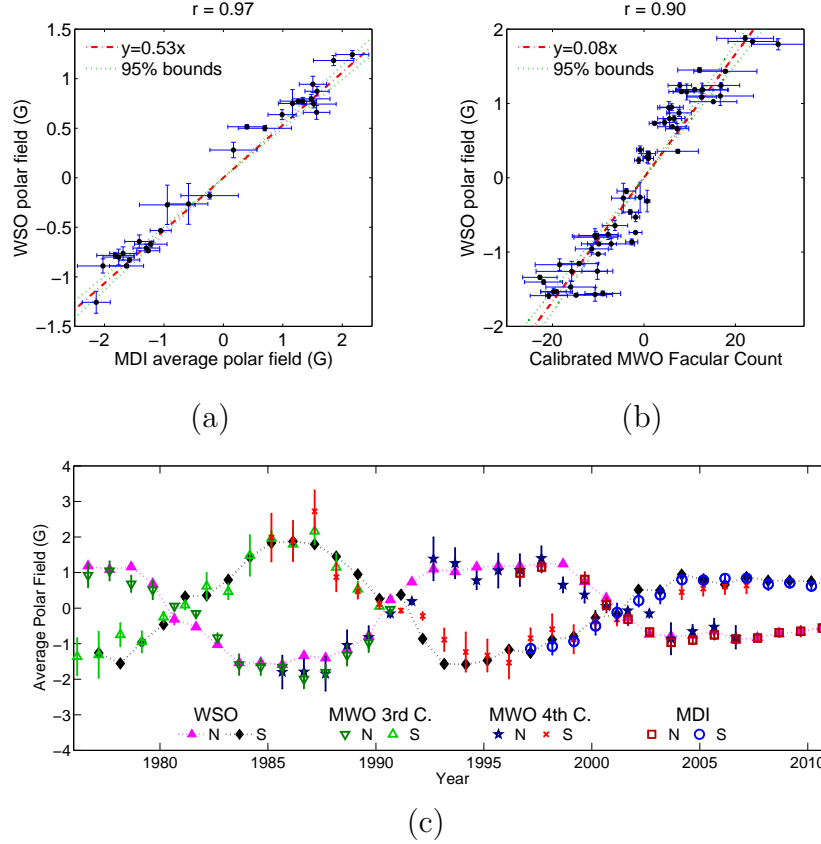
Fig. 11.— (a) Scatter plot comparing MDI average polar field with WSO measurements of the polar field. (b) Scatter plot comparing MWO facular measurements with WSO measurements of the polar field. Each scatter plot is fitted with a line passing through the origin (dot-dashed red) and the 95% confidence interval is bounded by dotted green lines. (c) Overplot of the WSO polar field measurements (dotted lines plus solid triangles-NP, diamonds-SP), the MWO calibrated facular measurements of the 3rd campaign (open downward-NP, upward-SP triangles), the 4th campaign (stars-NP, crosses-SP), and the corrected MDI average polar field (open squares-NP, circles-SP). MWO facular measurements are converted to polar field strength using a multiplication factor of 0.08 ± 0.01 G and the MDI average polar field is multiplied by a factor of 0.53 ± 0.03. Both correspond to the slopes and the 95% confidence interval of their respective linear fits (panels a and b).
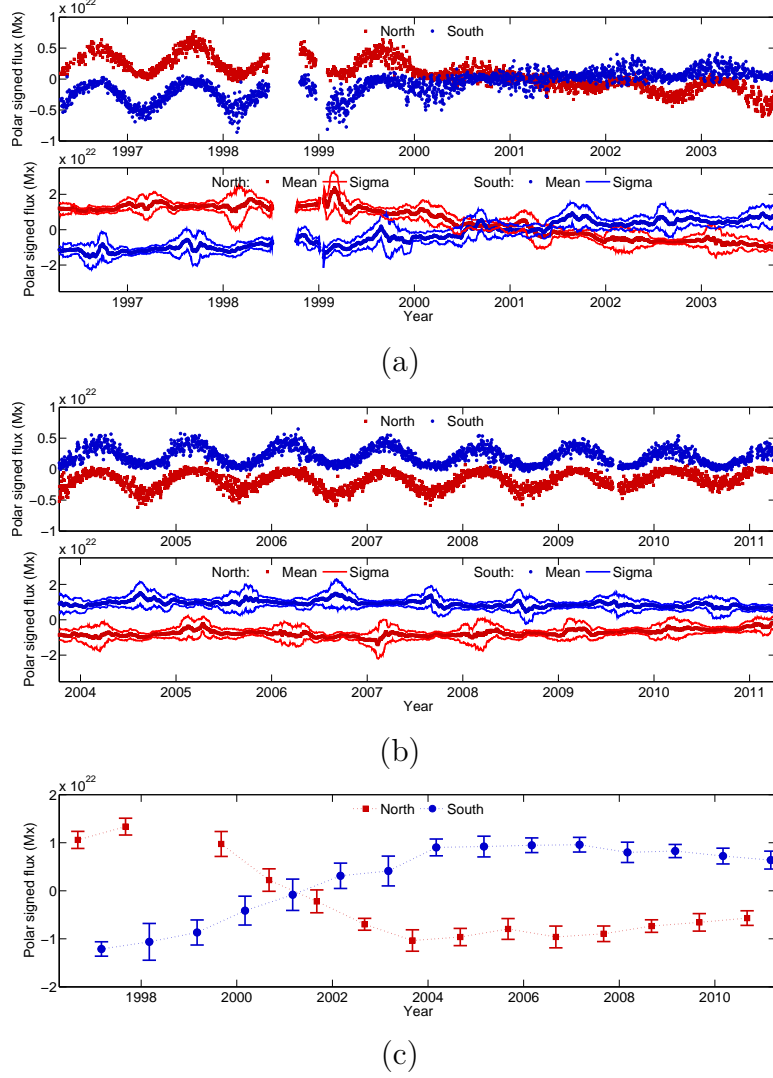
Fig. 12.— MDI total signed polar flux above (below) 70° (-70°) for the 1996-2004 (a) and 2004-2011 (b) intervals. The top panel of each figure shows the observed daily polar signed flux; the bottom panel shows polar flux after it has been corrected for the unseen backside area and then smoothed using a month-long running average. Red (blue) corresponds to the north (south) pole and the thin lines correspond to one standard deviation. (c) Selected values of the average signed polar flux for the 1996-2011 interval. Points corresponding to the 4-Mar (4-Sep) of each year are used for the south (north) pole. These dates correspond to the point in Earth's orbit with the best observations of each particular pole.
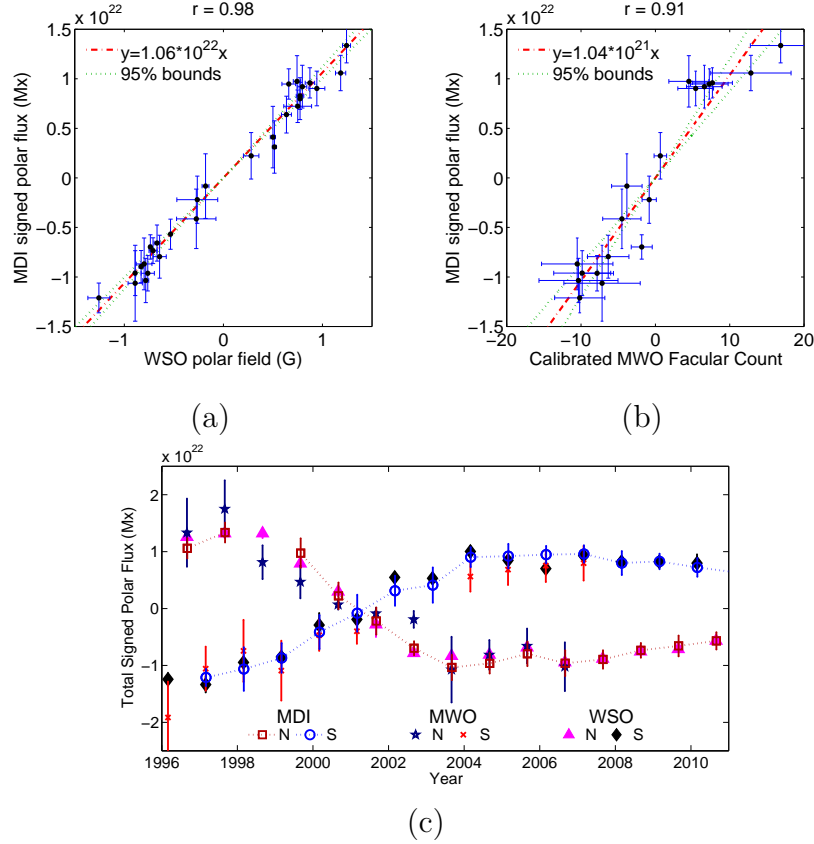
Fig. 13.— (a) Scatter plot comparing WSO measurements of the polar field with MDI signed polar flux. (b) Scatter plot comparing MWO facular measurements with MDI signed polar flux. Each scatter plot is fitted with a line passing through the origin (dot-dashed red) and the 95% confidence interval is bounded by dotted green lines. (c) Overplot of the MDI signed polar flux (dotted lines plus open squares-NP, circles-SP), MWO calibrated facular measurements (stars-NP, crosses-SP), and WSO polar field measurements (solid triangles-NP, diamonds-SP). MWO facular measurements are converted to polar field strength using a multiplication factor of $(1.04 \pm 0.16) \times 10^{21}$Mx and the WSO polar field measurements are multiplied by a factor of $(1.06 \pm 0.06) \times 10^{22}$Mx/G. Both correspond to the slopes and the 95% confidence interval of their respective linear fits (panels a and b).
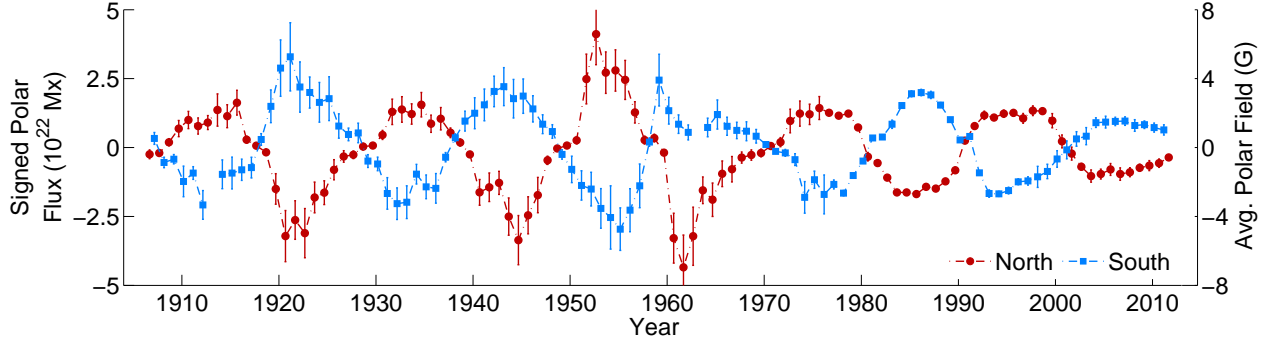
Fig. 14.— Consolidated signed polar flux database referenced to MDI measurements. Datapoints were taken from MDI (1996-2010), WSO (1975-1996), and MWO (1906-1975). The second axis shows the equivalent values of average polar field strength referenced to WSO measurements.
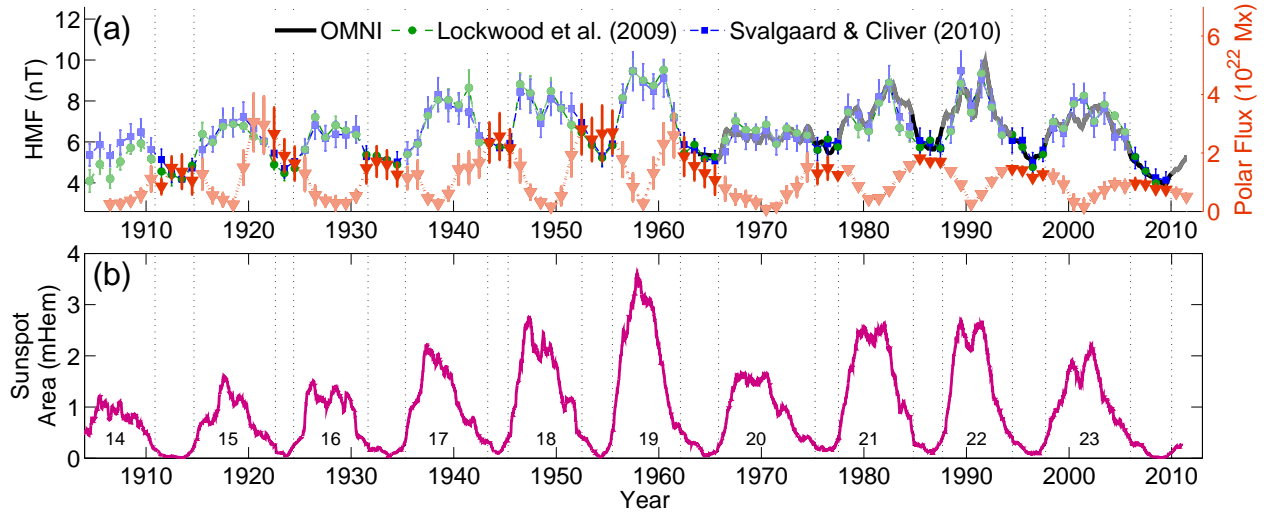

Fig. 15.— (a) Overplot of the HMF taken from the OMNI database (black solid line), the reconstructed HFM of Lockwood, Rouillard & Finch (2009; dashed line with circles), Svalgaard & Cliver (2010; dot-dashed line with squares) and the average of the polar flux amplitude in both hemispheres (dotted line with triangles). (b) Yearly smoothed total sunspot area of Balmaceda et al. (2009). Vertical dashed lines bracket intervals corresponding to sunspot minima. In the top panel colors are also accentuated during minima.
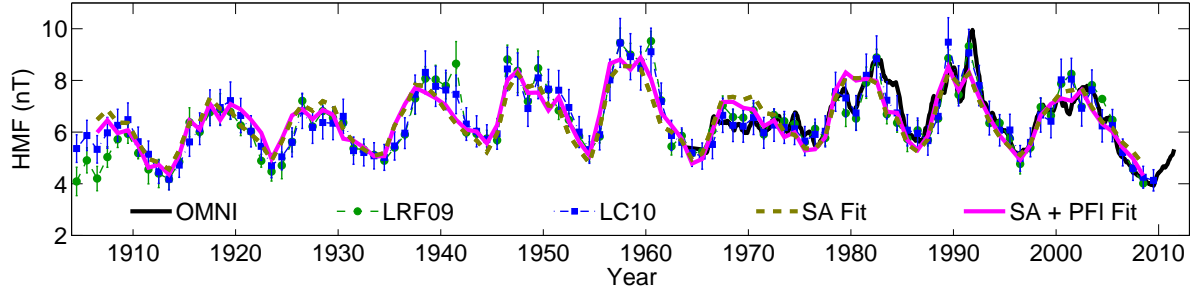
Fig. 16.— Overplot of the HMF taken from the OMNI database (black solid line), the recon-structed HFM of Lockwood, Rouillard & Finch (2009; dashed line with circles), Svalgaard & Cliver (2010; dot-dashed line with squares), the least-squares fit to the square root of sunspot area (thick dashed line) and the least-squares fit to a linear combination of the square root of sunspot area and the average of the polar flux amplitude in both hemispheres (thick solid magenta line).